

## Article

# Boron Nitride Thin Films with Anisotropic Optical Properties from Microscale Particle Density Distributions

Lyubov V. Kotova <sup>1,2</sup>, Linar A. Altynbaev <sup>1</sup>, Maria O. Zhukova <sup>2</sup>, Bogdan R. Borodin <sup>1</sup>,  
Vladimir P. Kochereshko <sup>1</sup>, Anna Baldycheva <sup>3,\*</sup> and Benjamin T. Hogan <sup>3,4</sup>

<sup>1</sup> Ioffe Institute, 194021 St. Petersburg, Russia

<sup>2</sup> Faculty of Photonics, ITMO University, 197101 St. Petersburg, Russia

<sup>3</sup> Department of Engineering, University of Exeter, Exeter EX4 4QF, UK

<sup>4</sup> Department of Electrical and Information Engineering, University of Oulu, 90014 Oulu, Finland

\* Correspondence: a.baldycheva@exeter.ac.uk

**Abstract:** Unusual optical anisotropy was experimentally observed in hexagonal boron nitride thin films produced from bulk boron nitride via ultrasonication. Both the linear and circular polarisation demonstrated a well-defined single axis of anisotropy over a large sample area. To understand this phenomenon, we employed statistical analysis of optical microscopy images and atomic force microscopy to reveal an ordered particle density distribution at the microscopic level corresponding to the optical axis observed in the polarisation data. The direction of the observed ordering matched the axis of anisotropy. Hence, we attribute the measured optical anisotropy of the thin films to microscopic variations in the particle density distribution.

**Keywords:** boron nitride; polarisation; optical anisotropy



**Citation:** Kotova, L.V.; Altynbaev, L.A.; Zhukova, M.O.; Borodin, B.R.; Kochereshko, V.P.; Baldycheva, A.; Hogan, B.T. Boron Nitride Thin Films with Anisotropic Optical Properties from Microscale Particle Density Distributions. *Coatings* **2022**, *12*, 1571. <https://doi.org/10.3390/coatings12101571>

Academic Editors: Piotr Potera and Torsten Brezesinski

Received: 25 August 2022

Accepted: 10 October 2022

Published: 18 October 2022

**Publisher's Note:** MDPI stays neutral with regard to jurisdictional claims in published maps and institutional affiliations.



**Copyright:** © 2022 by the authors. Licensee MDPI, Basel, Switzerland. This article is an open access article distributed under the terms and conditions of the Creative Commons Attribution (CC BY) license (<https://creativecommons.org/licenses/by/4.0/>).

## 1. Introduction

Interest in atomically thin (2D) materials has increased exponentially since the unique properties of graphene were first reported. Since then, researchers have extended the family of known 2D materials to include MXenes [1,2], transition metal dichalcogenides [3], and (of interest herein) hexagonal boron nitride (*h*-BN) [4,5] amongst others [6]. The optical properties of 2D materials can diverge significantly from those of the bulk crystal, opening up new avenues for their application [6–8]. For example, these materials are already being used to create a wide variety of new optoelectronic devices operating at wavelengths across the electromagnetic spectrum [6]. The diverse properties exhibited by the range of known 2D materials, combined with their ultrathin nature, give rise to the prospect of creating van der Waals heterostructures, in which different two-dimensional materials are stacked layer-by-layer to form composite materials with a fine degree of control over the desired properties [9]. Due to the contrasting strong intralayer covalent bonding and relatively weak interlayer interactions, van der Waals heterostructures retain many properties of the individual layer materials. However, the required precise nanoscale stacking is both time and cost intensive, limiting the scalability to large area devices [10,11]. In cases where large area devices are required, other methods and techniques for adjusting the optical properties could be advantageous.

2D materials can generally be synthesised by two overarching routes: top-down and bottom-up [12–15]. Bottom up methods (such as chemical vapour deposition [16] or molecular beam epitaxy [17]) can produce high quality 2D materials over relatively large areas, but are time-consuming, energy-intensive, and cost-prohibitive [14]. Top-down methods involve exfoliation of the bulk crystal [18,19]. The simplest technology for exfoliating bulk crystals is mechanical cleavage of the layers using sticky tape, as used in the first demonstrations of graphene [20]. This method can produce monolayer single crystals with very few defects [20]. However, the size of the individual monolayer

flakes is generally small and the yield low, such that the method cannot be easily scaled to mass production [12]. Hence, new methods for top-down synthesis are required that can overcome these respective fabrication barriers. One of the most promising developing technologies is the cleavage of thin layers from a bulk crystal using ultrasonication in a liquid [21–23]. This method can be easily applied to bulk crystals where the interlayer interactions are weaker than the intralayer [21]. The bulk crystals are dispersed in a solvent through which ultrasonic waves are propagated. The energy of the ultrasonic waves causes cavitation to occur within the bulk crystal, resulting in the delamination as the layers are pushed apart [21]. The result is a solution containing flakes of different sizes and thicknesses which can then be further separated by centrifugation and fractionation of the solution. Ultrasonication does not require the high temperatures typical in bottom-up syntheses, making the technique more energy and cost efficient [21]. While the bulk to 2D yield is generally relatively low, ultrasonication can be readily scaled up to produce larger quantities of 2D material overall [21]. However, while large quantities of 2D material can be produced relatively easily via ultrasonication, the individual particle sizes and shapes are hard to control without severely compromising the yield (e.g., by initiating a highly selective centrifugation/fractionation procedure) [24]. Additionally, the average size of the exfoliated particles is significantly less than the original bulk crystal(s) [21,23]. Hence, to produce large area devices using ultrasonicated 2D materials, it is necessary to fabricate thin films of the individual exfoliated particles of similar size and shape, that are uniformly distributed [23–26].

In this paper, we consider the case of boron nitride. The mechanical properties of boron nitride, such as high hardness [27] and high resistance to extreme temperatures and pressures [28,29], have already been widely exploited. In particular, boron nitride films can be used to make a range of composite materials [27,30]. Their low frictional wear and high flexibility [31] make them excellent candidates for the development of various flexible devices. For reduction to a 2D material, the hexagonal form of boron nitride is the obvious candidate. Bulk *h*-BN has a similar layered structure to graphite. Since the interlayer interactions in *h*-BN are weak compared to the intralayer covalent bonding, their cleavage can be induced relatively easily. Hence, *h*-BN can be readily exfoliated to give thinner crystals (down to the monolayer limit). Monolayer (2D) *h*-BN is stable with a graphene-like hexagonal lattice structure consisting of alternating boron and nitrogen atoms (see Figure 1a).

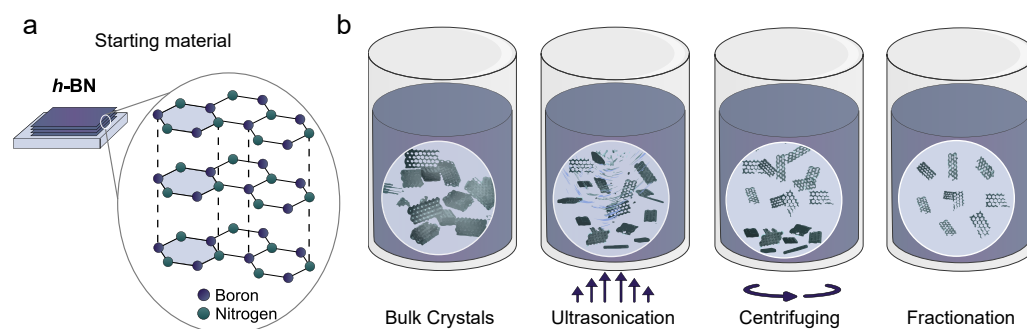


**Figure 1.** (a) The bulk *h*-BN structure with dashed lines showing the weaker interlayer van der Waals bonding. (b) The *h*-BN exfoliation procedure: a powder of bulk *h*-BN crystals is dispersed in a mixture of isopropanol and deionised water, the solution is ultrasonicated to induce cleavage of the interlayer bonds, then centrifuged to agglomerate the larger (residual bulk) particles, and finally the supernatant containing the suitably exfoliated particles is extracted by fractionation.

*h*-BN is an attractive material for barrier or passivation layers as it is one of the strongest known electrically-insulating materials, with significant prospects for use in nanoelectronics [32] and optoelectronics [33]. However, a significant barrier to its adoption in devices has been the scalability of methods for its synthesis [5]. We address the

scalability of the synthesis of *h*-BN by applying a top-down fabrication method based on ultrasonication which can produce highly uniform thin films at a large scale. Preliminary investigations using optical polarisation characterisation of the fabricated thin films demonstrated their optical anisotropy over the whole sample area with a single optical axis [34,35]. However, the anisotropy does not originate from any properties of the individual, chaotically-oriented particles.

To understand this phenomenon, we employ statistical analysis of optical microscopy images and atomic force microscopy to reveal an ordered particle density distribution at the microscopic level corresponding to the optical axis observed in the polarisation data. Hence, we attribute the measured optical anisotropy of the thin films to microscopic variations in the particle density distribution. This suggests that there is an opportunity to tune the optical properties of the thin films through defined ordering of the particle density distributions at the microscale or below, as a scalable, low-cost alternative to producing heterostructures.

## 2. Materials and Methods

### 2.1. Sample Preparation

*h*-BN thin films were prepared on polyethylene terephthalate (PET) substrates by the following method (Figure 1b). Bulk crystal *h*-BN powder (25 g) was initially dispersed in a beaker containing 500 mL of a 60:40 ratio mixture of isopropanol and deionised water [36–38]. The dispersion was ultrasonicated in a 120 W ultrasonic bath filled with deionised water at an initial temperature of 298 K. Five hour-long periods of ultrasonication, separated by 30 min each to prevent excessive heating of the solvent (over each one hour run, the temperature of the bath increased to around 318 K, which returned to around 298 K after the period of inactivity), to ensure a sufficient exfoliation yield from the bulk crystals. The partially exfoliated dispersion was then put through a centrifuging process for 10 min at 2000 rpm to sediment out the residual bulk material and larger particles, narrowing the distribution of particle sizes present in the supernatant and favouring thinner particles. The dispersion was fractionated to extract the supernatant, ensuring only suitably sized particles remained. The supernatant was then dried under vacuum (0.1 atm, 343 K) in a Schlenk line to fully remove the solvent mixture. 606 mg of the resulting powder was then redispersed in 12 mL of isopropanol mixed with 8 mL of deionised water to give a solution with a known concentration of around 30 mg/mL. This redispersed solution was ultrasonicated for a further 30 min to ensure a uniform dispersion. The redispersed solution was filtered through a microporous (~0.2 µm pores) PTFE (polytetrafluoroethylene) membrane to produce homogeneous thin films from the exfoliated *h*-BN. High quality films have been successfully developed using other two-dimensional materials (for example from dispersions of graphene oxide and molybdenum disulfide [23,39,40]), but not previously for *h*-BN. The thin films produced from filtering of the dispersion was achieved in accordance with a previously described method [22,25], marking a facile and scaleable method towards large-scale integration of the two-dimensional material. The membrane holding the thin film was carefully transferred to the desired (PET) substrate, with the side with the filtered *h*-BN in contact with the substrate surface. Isopropanol was used to wet the membrane. The substrate was then heated to 343 K to evaporate the isopropanol and simultaneously release the *h*-BN film from the membrane. The membrane was then removed leaving the thin film supported on the substrate.

### 2.2. Optical Measurements

The polarised light transmission spectra of the samples were recorded at room temperature using a 0.5 m monochromator (Princeton Instruments, Trenton, NJ, USA) with a 1200/mm grating equipped with a charge-coupled device detector using an established experimental technique [41,42]. A halogen lamp was used as the light source. A parallel beam of light was formed using lenses and slits. The sample holder allowed the unrestricted

rotation of the sample around the normal axis to obtain the dependencies of transmitted light polarisation state on the orientation of the incidence plane relative to the sample surfaces. The same setup was also used to measure the polarisation properties of the samples. The polarisation was controlled using half-wave and quarter-wave plates and a Glan-Taylor prism installed in the detecting part. Different polarisation configurations were measured in the visible spectral range. The incident light was linearly polarised. Spectral dependencies of the transmitted light intensity  $I(\omega)$  were investigated using two circularly polarised intensities  $I_{\sigma_{\pm}}$ , two linearly polarised intensities  $I_{\perp, \parallel}$ , and two linear components with axes rotated by  $\pm 45^\circ$  relative to the plane of incidence  $I_{1,2}$ . The polarisation degree of the transmitted light was determined using the Stokes parameters. The accuracy of the measured value of polarisation was estimated as 1%.

### 2.3. Optical Microscopy

We used an optical microscope capable of performing measurements in various polarisations to visualise the surface of the structures under investigation. Images of the samples' surface were obtained from bright-field microscopy using a Nikon ECLIPSE LV150 (Nikon Europe, Amsterdam, Netherlands) industrial microscope. The experimental images are presented in Figure 2b.

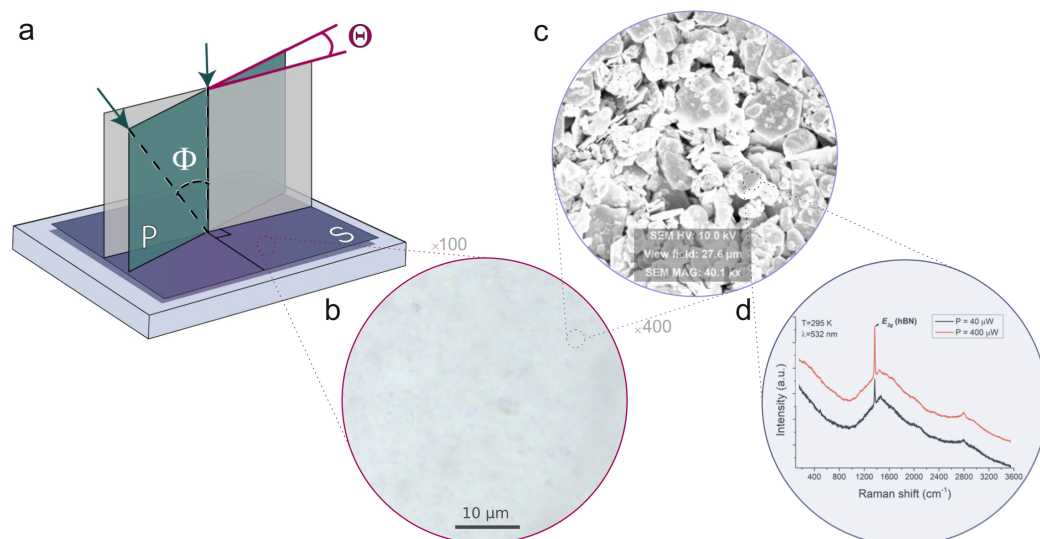


**Figure 2.** (a) The experimental scheme. P is the plane of incidence, S is the sample surface,  $\Phi$  is the angle of incidence, and  $\Theta$  is the azimuthal angle between the plane of incidence and the edge of the sample. Images of the sample surface taken with: (b) an optical microscope at  $\times 100$  magnification, and (c) a scanning electron microscope at  $\times 40,100$  magnification. Scale bars are shown in the images. (d) Raman spectrum of the sample under study at two excitation powers.

### 2.4. Scanning Electron Microscopy (SEM)

SEM images were obtained using a Tescan VEGA3 (TESCAN, Brno, Czech Republic) electron microscope operating at an accelerating voltage of 10 kV. Experimental images are presented in Figure 2c.

### 2.5. Raman Spectroscopy

Raman measurements were carried out using a Horiba Jobin-Yvon T64000 spectrometer (Horiba OOO, Moscow, Russia) equipped with a confocal microscope and a silicon CCD detector. Use of an objective lens with a  $100\times$  magnification and a NA of 0.9 together with a 1800 gr/mm grating allowed us to obtain Raman signal at room temperature with high spectral resolution from an area of  $\sim 1 \mu\text{m}$  in diameter. The measurements were performed with continuous-wave (cw) excitation using the 532 nm laser line of a Nd:YAG laser (Laser Quantum Torus, Stockport, UK). Experimental images are presented in Figure 2d.

### 2.6. Atomic Force Microscopy (AFM)

AFM was used to study the topography and the number of layers (thickness) of individual cleaved flakes on the surface, and also the topography and relief of the overall film surface. AFM investigation was performed using an Ntegra Aura (NT-MDT, St. Petersburg, Russia) scanning probe microscope using Si probes (HANC, TipsNano, Tallinn, Estonia) with resonant frequency  $f_0 \approx 140$  kHz, spring constant  $k \approx 3.5$  N m<sup>-1</sup>, and tip curvature radius < 10 nm.

### 3. Results

Hexagonal boron nitride (*h*-BN) thin films were prepared on polyethylene terephthalate (PET) substrates from few-layer flakes of *h*-BN prepared by ultrasonication of bulk crystals (Figure 1b; see methods for more details). The average overall thickness of the obtained films (formed of individual stacked thin *h*-BN particles) was about 5 microns. Optical and scanning electron microscopy (SEM) images of the surfaces of the obtained samples are presented in Figure 2b,c, respectively. The sample consisted of thin crystalline platelets of *h*-BN with transverse sizes of up to 5 microns (established via SEM) and thicknesses of 1–10 monolayers (determined via AFM). Visually, individual platelets appeared to be chaotically distributed. There were no obvious selected directions on the sample surface at either the hundred-micron scale (optical microscopy) or the micron scale (electron microscopy). The Raman spectrum of the thin film indicated that the *h*-BN crystals did not contain impurities. At the same time, the intense background scattering observed indicated a high density of defects in the overall film (Figure 2d).

Optical microscopy (Figure 2b) demonstrated the matte appearance of the thin film on the substrate, arising due to strong Rayleigh light scattering from the surface. Rayleigh scattering spectra were measured, for linearly polarised light, as a function of incident angle ( $\Phi$ , see Figure 2a) in the range from 0 to  $\pm 45^\circ$  and the azimuthal angle ( $\Theta$ , see Figure 2a) in the full range from  $0^\circ$  to  $360^\circ$ . The spectra did not have any structure, except for one broad peak of 1 eV width at energy 1.7 eV. The intensity of the scattered light did not depend on the azimuthal angle  $\Theta$ . In the dependence on the incident angle  $\Phi$ , there were no qualitative differences between the spectra except for a change in total intensity. The lack of directional dependence of the Rayleigh scattering spectra is indicative of the chaotic orientation (and hence averaged intrinsic anisotropy) of the sample.

Polarised light transmission spectra of the samples were recorded at room temperature. There was strong absorption in the region within the *h*-BN bandgap at energies above 3 eV. No interference features were observed in the transparency range from  $\sim 1.3$  eV up to  $\sim 3.0$  eV, indicating that the sample thickness noticeably fluctuated at the scale of the light beam size ( $\sim 1$  mm).

The Stokes parameters  $P_{\text{circ}}$  and  $P_{\text{lin}}$  of the transmitted light in the transparency range of this sample were measured for linearly polarised incident light. The degree of circular polarisation  $P_{\text{circ}}$  is

$$P_{\text{circ}} = \frac{I_{\sigma_+} - I_{\sigma_-}}{I_{\sigma_+} + I_{\sigma_-}}, \quad (1)$$

where  $I_{\sigma_+}$  is the intensity of the transmitted light with right circular polarisation, and  $I_{\sigma_-}$  is the intensity of the transmitted light with left circular polarisation. The degree of linear polarisation  $P_{\text{lin}}$  is

$$P_{\text{lin}} = \frac{I_0 - I_{90}}{I_0 + I_{90}}, \quad (2)$$

where  $I_0$  is the intensity of the transmitted light with a linear polarisation state that coincides with that of the incident light, and  $I_{90}$  is the intensity of the transmitted light with a linear polarisation state orthogonal to that of the incident light.

Figure 3 shows the spectral dependencies of the degree of circular polarisation  $P_{\text{circ}}$  as a function of the azimuthal angle  $\Theta$  between the polarisation direction and the edge of

the sample at normal light incidence. When linearly polarised light passed through the sample, it acquired a circularly polarised component. The degree of circular polarisation is dependent on the azimuthal angle  $\Theta$ . At an energy of 2.36 eV, the degree of circular polarisation changed sign. At this energy, the sample was optically isotropic. The maximum value of circular polarisation occurred at an energy of 1.91 eV.

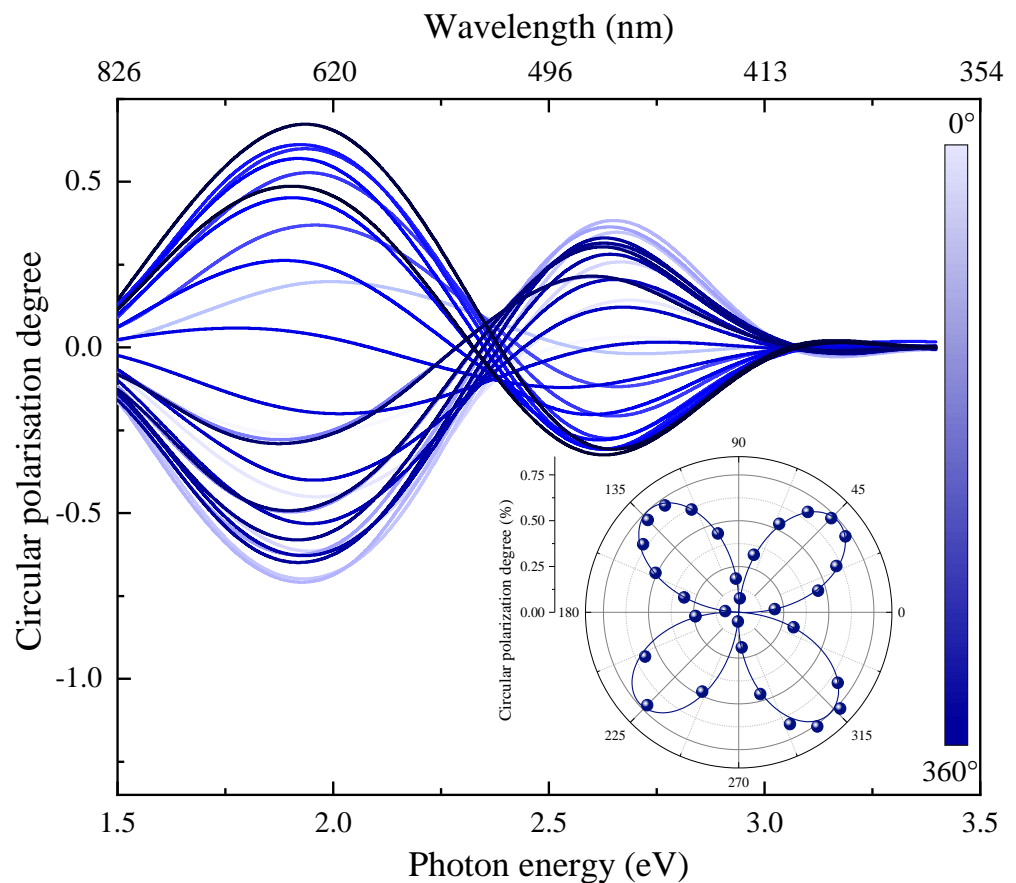


**Figure 3.** Spectral dependencies of the circular polarisation degree  $P_{\text{circ}}$  at azimuthal angles from  $0^\circ$  to  $360^\circ$  for the light passed through the sample when the incident light was linearly polarised. Spectra were obtained at room temperature. The insert shows the angular dependence of the polarisation conversion.

Figure 4 shows the spectral dependence of the degree of linear polarisation  $P_{\text{lin}}$  in the axes coinciding with the direction of polarisation of the incident light as a function of the azimuthal angle  $\Theta$ . For linear polarisation, similar dependencies to those for the circular polarisation were obtained with one difference: at energies where  $P_{\text{circ}}$  is maximal,  $P_{\text{lin}}$  is minimal. The magnitude of the degree of linear polarisation reached a maximum when the plane of polarisation coincided with the optical axis of the sample.

The data obtained demonstrated that the birefringence phenomenon was observed in the entire measured spectral range. This phenomenon manifests itself in the conversion of linear polarisation into circular polarisation. The birefringence was measured at different points on the sample surface. The direction of the optical axis was found not to change over the sample area ( $\sim 1 \text{ cm}^2$ ). The arrows in the inset of Figure 4 show the direction of the optical axis.

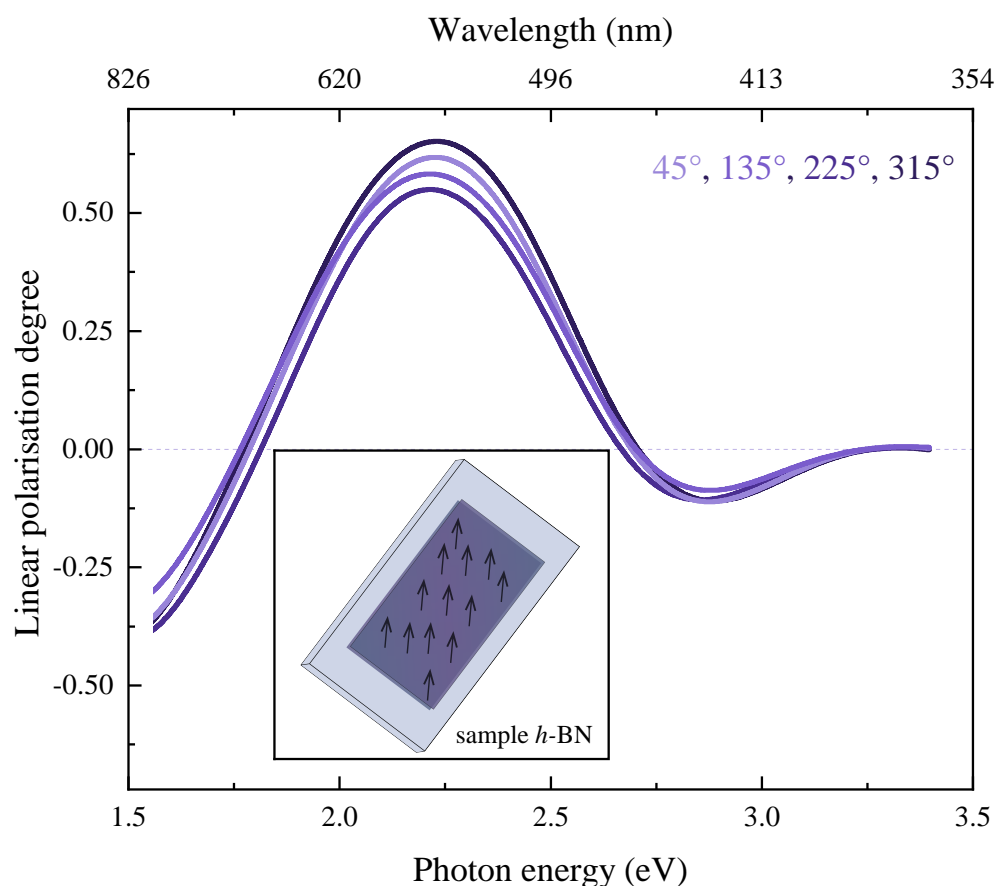


**Figure 4.** Spectral dependencies of the linear polarisation degree  $P_{lin}$  at selected azimuthal angles for linearly polarised light passed through the sample. Spectra were obtained at room temperature. The inset shows the direction of the optical axis over the entire area of the sample.

#### 4. Discussion

The optical axis in the polycrystalline sample could be the result of either of two causes: the anisotropy of the individual particles themselves or the anisotropy of their collective distribution [43]. Individual crystals of *h*-BN do indeed have optical anisotropy. The refractive indices of light along the hexagonal axis and perpendicular to it differ significantly [44]. However, as shown in Figure 2, the orientation of the microcrystals in the samples investigated herein is completely chaotic (at least at scales of a few up to hundreds of microns). Given this chaotic arrangement of the individual particles in the thin film, the anisotropy of the particles alone cannot lead to an overall anisotropy of the entire sample as the net effect of the varied orientations would lead to a negation on average (however, it could manifest as a local anisotropy). Thus, the observed birefringence with a single direction of the optical axis over the entire sample area ( $\sim 1 \text{ cm}^2$ ) cannot have been caused by the anisotropy of the *h*-BN microcrystals themselves. This indicates that the cause of anisotropy is not hidden in the properties of individual microcrystals but is common to the entire sample and manifests itself at large distances. It should also be noted that it was verified that the substrate itself was optically isotropic. Measurements of the reflected/scattered light from the sample show that, in contrast to the cases described in [41,42], the inclination of microcrystals in the samples considered herein is chaotic. The presence of a hidden order in a disordered substance may indicate that there is a small system of microcrystals in which there is no complete averaging of properties. However, this is not valid for our case since the anisotropy is observed consistently across a large surface area. Another reason may be the ordered arrangement of microcrystals, which manifests itself as optical

anisotropy. A similar case was theoretically modelled in [43] where no anisotropy was visible by eye, but anisotropic light scattering nevertheless occurred.

To describe the observed phenomenon, we can use the model of an effective dielectric medium [45–47]. Although the particle sizes in our case were comparable or larger than the wavelength of light and the applicability of this model is not entirely justified, the basic properties of the medium should be described at least qualitatively by this model.

We considered our sample as a composite with an effective permittivity  $\varepsilon_{eff}$  consisting of microcrystals and voids between them. We took the dielectric permittivity of boron nitride averaged over all orientations as an approximation of the dielectric permittivity of the ensemble of microcrystals  $\langle \varepsilon \rangle = \langle n \rangle^2$  [44]. We then used the Maxwell Garnett model [47] in its generalised form outlined by Bruggeman [48]. In this model, the permittivity of an effective medium  $\varepsilon_{eff}$  consisting of several components can be found as a solution of the equation

$$\sum_{(i=1)}^N f_i \theta_i (\varepsilon_{eff} - \varepsilon_i) = 0, \quad (3)$$

where  $\varepsilon_i$  is the dielectric permittivity of the components,  $f_i$  is the filling factor of the component  $i$ , and  $\theta_i$  is the form factor of the component  $i$ . The normalisation condition must also be met.

$$\sum_{(i=1)}^N f_i = 1, \quad \sum_{(i=1)}^N \theta_i = 1 \quad (4)$$

According to Equation (3), the anisotropy of the sample can be related both to the anisotropy of the dielectric permittivity of the microcrystals themselves and to the anisotropy of their distribution. For randomly-oriented microcrystals, the anisotropy of the sample can be associated only with the dependence of the filling factor on the direction (Equation (3)). Knowing the thickness of the sample and the spectral position of the isotropic points, we can determine the difference in refractive indices for ordinary and extraordinary beams.

$$\langle 2n \rangle (n_{eff}^\perp - n_{eff}^\parallel) = (n_{eff}^\perp)^2 - (n_{eff}^\parallel)^2 = \varepsilon_{eff}^\perp - \varepsilon_{eff}^\parallel. \quad (5)$$

From the data obtained, we can estimate the value of the anisotropy of the filling factor. The average thickness of the sample was estimated from the amount of deposited material to be 5 microns. Averaged in all directions the refractive index was taken as  $\langle n \rangle \approx 2$ . The presence of an optical axis means that ordinary and extraordinary rays propagate at different phase velocities. This is manifested in the conversion of linear polarisation into circular polarisation. If the thickness of the sample is such that the phase difference of these rays is  $N\pi$ , then there is no polarisation conversion. This is the isotropic point in the transmission spectrum. If the phase difference is  $(\pi/2 + N\pi)$ , then the conversion is maximal. Some variation in the spectral position of the isotropic point in Figure 3 occurred as the incident light beam spot shifted slightly over the surface area when the sample was rotated.

Hence, we found the difference in the effective refractive indices to be  $\varepsilon_{eff}^\perp - \varepsilon_{eff}^\parallel \approx 0.20$ . Assuming that the microcrystals were oriented completely chaotically, and the observed anisotropy was caused only by their spatial alignment, we obtain a filling factor of  $f^\perp - f^\parallel \approx 0.05$ . We emphasise that this was only an estimated value based on the outlined assumptions. Such a small value may not be noticeable by eye, but it is manifested in the transmission spectra.

We performed a statistical analysis of the surface image as described in [43]. Figure 2b clearly shows that there are light and dark spots on the surface of the sample. We inferred that the darker areas are associated with voids between microcrystals. The spatial dependence of the distribution of dark and light spots was analysed. The density of dark and light spots as a function of the azimuthal angle is shown in polar coordinates in Figure 5. The distribution density of the microcrystals was anisotropic, with an axis directed at an angle

of  $35^\circ$  relative to the edge of the sample. The direction of the anisotropy axis determined coincides with the direction of the axis determined from the polarisation measurements.

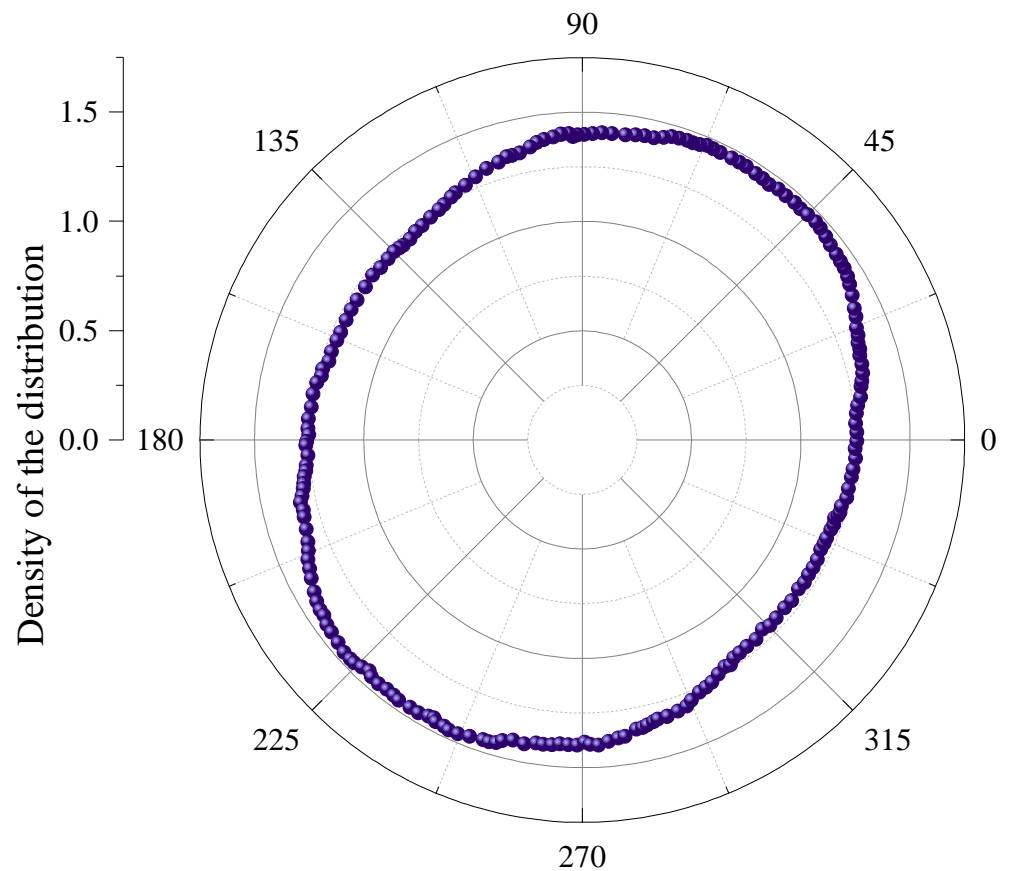


**Figure 5.** The relative density of the distribution of microcrystals, constructed by statistical analysis of the distribution of dark and light spots in Figure 2b.

The conclusion about the presence of a selected direction in the sample was confirmed using an atomic force microscope (AFM). The large-scale anisotropy of the microcrystal distribution density is clearly visible in AFM images of the surface (see Figure 6). The image clearly shows wide dark stripes directed at an angle of about  $30^\circ$  with respect to the horizontal (defined as parallel to the edge of the sample). Owing to the great height of flakes that make up the surface, the thin structure of the surface could not be revealed. The thin, bright, narrow, horizontal furrows along the scanning direction are not connected with the real structure of the surface but appeared due to the inertia of the measuring system. However, it can be clearly seen that the microcrystals formed hills (light stripes) and valleys (dark stripes) of density on a macroscopic scale.

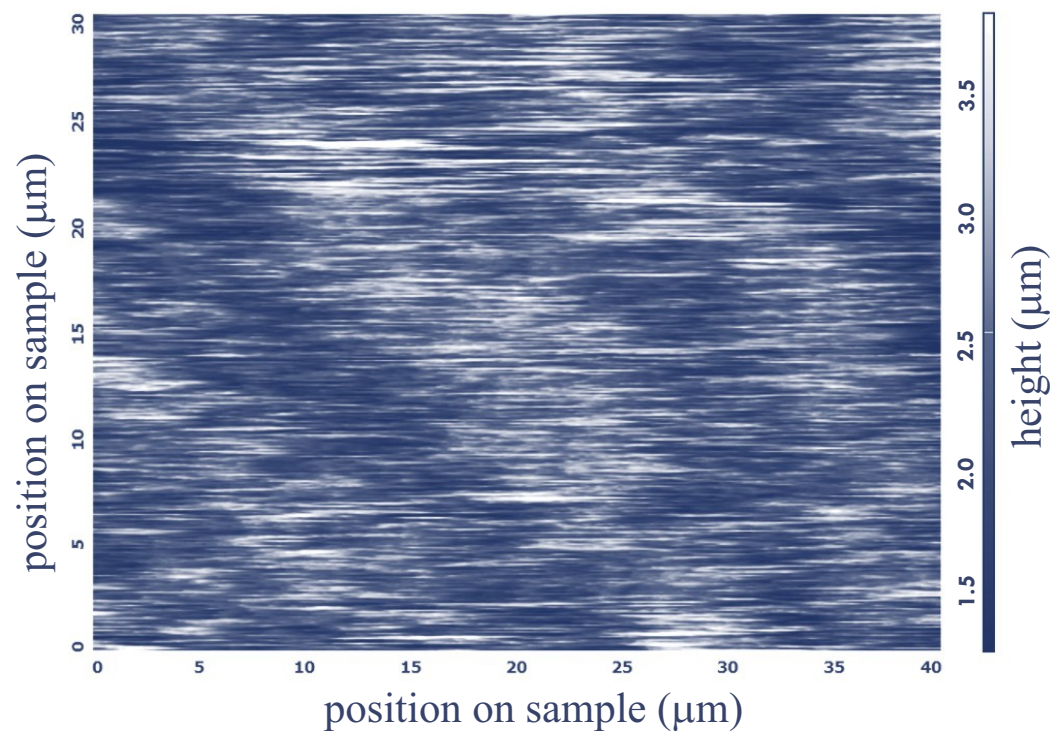


**Figure 6.** Image of the sample surface obtained using an atomic force microscope. The image size is  $30 \times 40$  microns. The deep blue-to-white contrast scale bar spans a range of  $4 \mu\text{m}$ .

A possible reason for the formation of the macroscopic ordering is the electrostatics of the exfoliated microcrystals. When we exfoliate the bulk *h*-BN crystals in the ultrasonic bath, the resulting microcrystals have an electrostatic difference between the edges where intralayer covalent bonds are broken and the planar surfaces where only weak van der Waals bonding is broken [23]. They should then preferably agglomerate in an ordered manner in accordance with the direction of their dipole moments during filtering and transfer to the substrate. Due to such anisotropic correlations in the distribution of microcrystals, their density in different directions may be different. This may be invisible to the eye (see Figure 1a in [43]), but it may manifest in the polarisation properties. Indeed, the presence of such electrostatic fields may be sufficient for their ordering at large distances.

## 5. Conclusions

The transmission and reflection spectra of thin films formed of agglomerated individual *h*-BN microcrystals were studied in the transparency range below the edge of the fundamental absorption band. The spectral dependencies of the linear and circular polarisation of light passing through the sample were measured. Optical and scanning electron microscopy showed the absence of noticeable selected directions in the sample. However, birefringence was observed in the study of the Stokes parameters of light that passed through the sample. It was established that the optical axes were unidirectional over the entire sample area. Simultaneously, the diffused light from the sample was not polarised. This indicated that the cause of the anisotropy was not in the properties of individual microcrystals but was common for the entire sample. Statistical analysis of optical images of the sample confirmed that the thin films demonstrate microscopic ordering of their density distributions in the same direction as the optical axis, giving rise to the observed optical anisotropy. This conclusion was further supported by AFM images of the sample surface. This suggests that there is an opportunity to tune the optical properties of the thin films through defined ordering of the particle density distributions at the microscale or below, as a scalable, low-cost alternative to producing heterostructures.

**Author Contributions:** Experiments, L.V.K., L.A.A., M.O.Z. and B.R.B.; sample fabrication, B.T.H. and A.B.; data curation, L.V.K.; writing—original draft preparation, L.V.K.; writing—review and editing, B.T.H., L.V.K. and A.B.; visualization, L.V.K.; supervision, A.B. and V.P.K. All authors have read and agreed to the published version of the manuscript.

**Funding:** This research was funded by: Engineering and Physical Sciences Research Council (EPSRC) of the United Kingdom (Grant No. EP/N035569/1); EPSRC Centre for Doctoral Training in Electromagnetic Metamaterials (Grant No. EP/L015331/1); Russian Science Foundation (project No. 21-12-00304).

**Institutional Review Board Statement:** Not applicable.

**Informed Consent Statement:** Not applicable.

**Data Availability Statement:** The underlying data represented in this paper are in the public domain. Additional data can be obtained from the authors upon reasonable request.

**Conflicts of Interest:** The authors declare no conflict of interest. The funders had no role in the design of the study; in the collection, analyses, or interpretation of data; in the writing of the manuscript; or in the decision to publish the results.

## Abbreviations

The following abbreviations are used in this manuscript:

2D	two-dimensional
<i>h</i> -BN	hexagonal boron nitride
PET	polyethylene terephthalate
PTFE	polytetrafluoroethylene
SEM	scanning electron microscopy
AFM	atomic force microscopy

## References

1. Xu, J.; Peng, T.; Qin, X.; Zhang, Q.; Liu, T.; Dai, W.; Chen, B.; Yu, H.; Shi, S. Recent advances in 2D MXenes: Preparation, intercalation and applications in flexible devices. *J. Mater. Chem. A* **2021**, *9*, 14147–14171. [[CrossRef](#)]
2. Pang, J.; Mendes, R.G.; Bachmatiuk, A.; Zhao, L.; Ta, H.Q.; Gemming, T.; Liu, H.; Liu, Z.; Rummeli, M.H. Applications of 2D MXenes in energy conversion and storage systems. *Chem. Soc. Rev.* **2019**, *48*, 72–133. [[CrossRef](#)]
3. Manzeli, S.; Ovchinnikov, D.; Pasquier, D.; Yazyev, O.V.; Kis, A. 2D transition metal dichalcogenides. *Nat. Rev. Mater.* **2017**, *2*, 17033. [[CrossRef](#)]
4. Rasul, M.G.; Kiziltas, A.; Arfaei, B.; Shahbazian-Yassar, R. 2D boron nitride nanosheets for polymer composite materials. *npj 2D Mater. Appl.* **2021**, *5*, 56. [[CrossRef](#)]
5. Zhang, K.; Feng, Y.; Wang, F.; Yang, Z.; Wang, J. Two dimensional hexagonal boron nitride (2D-hBN): Synthesis, properties and applications. *J. Mater. Chem. C* **2017**, *5*, 11992–12022. [[CrossRef](#)]
6. Khan, K.; Tareen, A.K.; Aslam, M.; Wang, R.; Zhang, Y.; Mahmood, A.; Ouyang, Z.; Zhang, H.; Guo, Z. Recent developments in emerging two-dimensional materials and their applications. *J. Mater. Chem. C* **2020**, *8*, 387–440. [[CrossRef](#)]
7. Catania, F.; Marras, E.; Giorcelli, M.; Jagdale, P.; Lavagna, L.; Tagliaferro, A.; Bartoli, M. A Review on Recent Advancements of Graphene and Graphene-Related Materials in Biological Applications. *Appl. Sci.* **2021**, *11*, 614. [[CrossRef](#)]
8. Tielrooij, K.J. Ultrafast light-based logic with graphene. *Nat. Mater.* **2022**, *1–2*. [[CrossRef](#)] [[PubMed](#)]
9. Geim, A.; Grigorieva, I. Van der Waals heterostructures. *Nature* **2013**, *499*, 419–425. [[CrossRef](#)] [[PubMed](#)]
10. Liu, L.; Zhai, T. Wafer-scale vertical van der Waals heterostructures. *InfoMat* **2021**, *3*, 3–21. [[CrossRef](#)]
11. Fan, S.; Vu, Q.A.; Tran, M.D.; Adhikari, S.; Lee, Y.H. Transfer assembly for two-dimensional van der Waals heterostructures. *2D Mater.* **2020**, *7*, 022005. [[CrossRef](#)]
12. Guo, B.; Xiao, Q.L.; Wang, S.h.; Zhang, H. 2D Layered Materials: Synthesis, Nonlinear Optical Properties, and Device Applications. *Laser Photonics Rev.* **2019**, *13*, 1800327. [[CrossRef](#)]
13. Xiao, X.; Wang, H.; Urbankowski, P.; Gogotsi, Y. Topochemical synthesis of 2D materials. *Chem. Soc. Rev.* **2018**, *47*, 8744–8765. [[CrossRef](#)] [[PubMed](#)]
14. Mannix, A.J.; Kiraly, B.; Hersam, M.C.; Guisinger, N.P. Synthesis and chemistry of elemental 2D materials. *Nat. Rev. Chem.* **2017**, *1*, 0014. [[CrossRef](#)]
15. Karfa, P.; Chandra Majhi, K.; Madhuri, R. Chapter 2—Synthesis of two-dimensional nanomaterials. In *Two-Dimensional Nanostructures for Biomedical Technology*; Khan, R., Barua, S., Eds.; Elsevier: Amsterdam, The Netherlands, 2020; pp. 35–71. [[CrossRef](#)]

16. Shen, P.C.; Lin, Y.; Wang, H.; Park, J.H.; Leong, W.S.; Lu, A.Y.; Palacios, T.; Kong, J. CVD Technology for 2-D Materials. *IEEE Trans. Electron Devices* **2018**, *65*, 4040–4052. [[CrossRef](#)]
17. Seredyński, B.; Ogorzałek, Z.; Zajkowska, W.; Bożek, R.; Tokarczyk, M.; Suffczyński, J.; Kret, S.; Sadowski, J.; Gryglas-Borysiewicz, M.; Pacuski, W. Molecular Beam Epitaxy of a 2D Material Nearly Lattice Matched to a 3D Substrate: NiTe<sub>2</sub> on GaAs. *Cryst. Growth Des.* **2021**, *21*, 5773–5779. [[CrossRef](#)]
18. Ba, H.; Truong-Phuoc, L.; Pham-Huu, C.; Luo, W.; Baaziz, W.; Romero, T.; Janowska, I. Colloid Approach to the Sustainable Top-Down Synthesis of Layered Materials. *ACS Omega* **2017**, *2*, 8610–8617. [[CrossRef](#)]
19. Wang, X.Y.; Narita, A.; Müllen, K. Precision synthesis versus bulk-scale fabrication of graphenes. *Nat. Rev. Chem.* **2018**, *2*, 0100. [[CrossRef](#)]
20. Novoselov, K.S. Electric Field Effect in Atomically Thin Carbon Films. *Science* **2004**, *306*, 666–669. [[CrossRef](#)]
21. Niu, L.; Coleman, J.N.; Zhang, H.; Shin, H.; Chhowalla, M.; Zheng, Z. Production of Two-Dimensional Nanomaterials via Liquid-Based Direct Exfoliation. *Small* **2016**, *12*, 272–293. [[CrossRef](#)]
22. Jalili, R.; Aminorroaya-Yamini, S.; Benedetti, T.M.; Aboutalebi, S.H.; Chao, Y.; Wallace, G.G.; Officer, D.L. Processable 2D materials beyond graphene: MoS<sub>2</sub> liquid crystals and fibres. *Nanoscale* **2016**, *8*, 16862–16867. [[CrossRef](#)]
23. Hogan, B.T.; Kovalska, E.; Zhukova, M.O.; Yildirim, M.; Baranov, A.; Craciun, M.F.; Baldycheva, A. 2D WS<sub>2</sub> liquid crystals: Tunable functionality enabling diverse applications. *Nanoscale* **2019**, *11*, 16886–16895. [[CrossRef](#)] [[PubMed](#)]
24. Hogan, B.T.; Kovalska, E.; Craciun, M.F.; Baldycheva, A. 2D material liquid crystals for optoelectronics and photonics. *J. Mater. Chem. C* **2017**, *5*, 11185–11195. [[CrossRef](#)]
25. Shaban, P.; Oparin, E.; Zhukova, M.; Hogan, B.; Kovalska, E.; Baldycheva, A.; Tsyppkin, A. Transmission properties of van der Waals materials for terahertz time-domain spectroscopy applications. *AIP Conf. Proc.* **2020**, *2300*, 020111. [[CrossRef](#)]
26. Zhukova, M.; Hogan, B.; Oparin, E.; Shaban, P.; Grachev, Y.; Kovalska, E.; Walsh, K.; Craciun, M.; Baldycheva, A.; Tsyppkin, A. Transmission Properties of FeCl<sub>3</sub>-Intercalated Graphene and WS<sub>2</sub> Thin Films for Terahertz Time-Domain Spectroscopy Applications. *Nanoscale Res. Lett.* **2019**, *14*, 225. [[CrossRef](#)]
27. Brant, J.; Brunetta, C.; Aitken, J. 5.09 - Chalcogenides and Nonoxides. In *Comprehensive Inorganic Chemistry II (Second Edition)*, 2nd ed.; Reedijk, J., Poepelmeier, K., Eds.; Elsevier: Amsterdam, The Netherlands, 2013; pp. 213–283. [[CrossRef](#)]
28. Eichler, J.; Lesniak, C. Boron nitride (BN) and BN composites for high-temperature applications. *J. Eur. Ceram. Soc.* **2008**, *28*, 1105–1109. Engineering Ceramics '07: From Engineering To Functionality. [[CrossRef](#)]
29. Kostoglou, N.; Polychronopoulou, K.; Rebholz, C. Thermal and chemical stability of hexagonal boron nitride (h-BN) nanoplatelets. *Vacuum* **2015**, *112*, 42–45. [[CrossRef](#)]
30. Joy, J.; George, E.; Haritha, P.; Thomas, S.; Anas, S. An overview of boron nitride based polymer nanocomposites. *J. Polym. Sci.* **2020**, *58*, 3115–3141. [[CrossRef](#)]
31. Song, W.L.; Wang, P.; Cao, L.; Anderson, A.; Mezziani, M.J.; Farr, A.J.; Sun, Y.P. Polymer/Boron Nitride Nanocomposite Materials for Superior Thermal Transport Performance. *Angew. Chem. Int. Ed.* **2012**, *51*, 6498–6501. [[CrossRef](#)]
32. Moon, P.; Koshino, M. Electronic properties of graphene/hexagonal-boron-nitride moiré superlattice. *Phys. Rev. B* **2014**, *90*, 155406. [[CrossRef](#)]
33. Ronning, C.; Banks, A.; McCarron, B.; Schlessler, R.; Sitar, Z.; Davis, R.; Ward, B.; Nemanich, R. Structural and electronic properties of boron nitride thin films containing silicon. *J. Appl. Phys.* **1998**, *84*, 5046–5051. [[CrossRef](#)]
34. Kotova, L.V.; Altyntbaev, L.A.; Zhukova, M.O.; Hogan, B.T.; Baldycheva, A.; Kurbatov, D.M.; Kochereshko, V.P. Anisotropy of Optical Properties of Hexagonal Boron Nitride Films. *Phys. Solid State* **2021**, *63*, 1437–1441. [[CrossRef](#)]
35. Kotova, L.V.; Altyntbaev, L.A.; Zhukova, M.O.; Hogan, B.T.; Baldycheva, A.; Kaliteevski, M.A.; Kochereshko, V.P. Anisotropic Optical Properties of Hexagonal Boron Nitride Films. *Bull. Russ. Acad. Sci. Phys.* **2022**, *86*, 813–816. [[CrossRef](#)]
36. Backes, C.; Higgins, T.M.; Kelly, A.; Boland, C.; Harvey, A.; Hanlon, D.; Coleman, J.N. Guidelines for Exfoliation, Characterization and Processing of Layered Materials Produced by Liquid Exfoliation. *Chem. Mater.* **2017**, *29*, 243–255. [[CrossRef](#)]
37. Coleman, J.N.; Lotya, M.; O'Neill, A.; Bergin, S.D.; King, P.J.; Khan, U.; Young, K.; Gaucher, A.; De, S.; Smith, R.J.; et al. Two-Dimensional Nanosheets Produced by Liquid Exfoliation of Layered Materials. *Science* **2011**, *331*, 568–571. [[CrossRef](#)]
38. Habib, T.; Sundaravadeivel Devarajan, D.; Khabaz, F.; Parviz, D.; Achee, T.C.; Khare, R.; Green, M.J. Cosolvents as Liquid Surfactants for Boron Nitride Nanosheet (BNNS) Dispersions. *Langmuir* **2016**, *32*, 11591–11599. [[CrossRef](#)]
39. Akbari, A.; Sheath, P.; Martin, S.; Shinde, D.; Shaibani, M.; Banerjee, P.; Tkacz, R.; Bhattacharyya, D.; Majumder, M. Large-area graphene-based nanofiltration membranes by shear alignment of discotic nematic liquid crystals of graphene oxide. *Nat. Commun.* **2016**, *7*, 10891. [[CrossRef](#)]
40. Fu, K.; Wang, Y.; Yan, C.; Yao, Y.; Chen, Y.; Dai, J.; Lacey, S.; Wang, Y.; Wan, J.; Li, T.; et al. Graphene Oxide-Based Electrode Inks for 3D-Printed Lithium-Ion Batteries. *Adv. Mater.* **2016**, *28*, 2587–2594. [[CrossRef](#)]
41. Kotova, L.; Platonov, A.; Poshakinsky, A.; Shubina, T. Polarization Conversion in MoS<sub>2</sub> Flakes. *Semiconductors* **2020**, *54*, 1509–1513. [[CrossRef](#)]
42. Kotova, L.V.; Rakhlin, M.V.; Galimov, A.I.; Eliseyev, I.A.; Borodin, B.R.; Platonov, A.V.; Kirilenko, D.A.; Poshakinsky, A.V.; Shubina, T.V. MoS<sub>2</sub> flake as a van der Waals homostructure: Luminescence properties and optical anisotropy. *Nanoscale* **2021**, *13*, 17566–17575. [[CrossRef](#)]
43. Jacucci, G.; Bertolotti, J.; Vignolini, S. Role of Anisotropy and Refractive Index in Scattering and Whiteness Optimization. *Adv. Opt. Mater.* **2019**, *7*, 1900980. [[CrossRef](#)]

44. Segura, A.; Artús, L.; Cuscó, R.; Taniguchi, T.; Cassabois, G.; Gil, B. Natural optical anisotropy of h-BN: Highest giant birefringence in a bulk crystal through the mid-infrared to ultraviolet range. *Phys. Rev. Mater.* **2018**, *2*, 024001. [[CrossRef](#)]
45. Thouless, D. Electrons in disordered systems and the theory of localization. *Phys. Rep.* **1974**, *13*, 93–142. [[CrossRef](#)]
46. Landauer, R. Electrical conductivity in inhomogeneous media. *Aip Conf. Proc.* **1978**, *40*, 2–45. [[CrossRef](#)]
47. Choy, T.C. *Effective Medium Theory: Principles and Applications*; Clarendon Press: Oxford, UK, 2016.
48. Bruggeman, D.A.G. Berechnung verschiedener physikalischer Konstanten von heterogenen Substanzen. I. Dielektrizitätskonstanten und Leitfähigkeiten der Mischkörper aus isotropen Substanzen. *Ann. Der Phys.* **1935**, *416*, 636–664. [[CrossRef](#)]